Nanoscale Chemical Analysis in Various Interfaces with Energy Dispersive X-Ray Spectroscopy and Transmission Electron Microscopy

Seiichiro Ii

National Institute for Materials Science
Japan

1. Introduction

The properties of materials strongly depend on their microstructure such factors as lattice defect type and density, size, distribution of phases present. During last half century, the development of transmission electron microscopy (TEM) has provided an advance in our understanding of the details of not only the microstructure but also the crystallographic feature of materials on a sub-micrometer scale (Edington, 1974; Fultz & Howe, 2002; Wiliams and Carter, 1996). On the other hand, many of materials generally consist of more than two elements and include impurities and those are applied to the industrial field. Abovementioned lattice defects in those alloys are one of preferential site of segregation of alloying elements and impurities. In order to clarify the mechanical and functional behaviors of the alloys, we should investigate not only the microstructure but also the elemental distribution of alloying elements and impurities. For latter purpose, TEM equipped with a spectroscope is considered to be one of powerful tool. Typical spectroscopes installed to TEM are energy dispersive X-ray spectroscopy (EDS), wavelength dispersive X-ray spectroscopy (WDS) and electron energy loss spectroscopy (EELS). These spectroscopes are utilized some signals resulting from an interaction between electron and specimen as shown in Fig. 1. For EDS, characteristic X-ray shown as red colored characters in Fig. 1 is analyzed. In this chapter, the EDS is focused. EELS is also one of important spectroscopy in TEM as well as EDS. The EELS is detected and analyzed an inelastic electron interacted with the specimen. EELS has an advantage for analysis of light elements such as B, C, N and O. Additionally, obtained EEL spectrum provides the chemical bonding information of the specimen. Details can be referred to some references (Brydson, 2001; Egerton, 1996). EDS combined with TEM is one of useful spectroscopy in the materials science and widely used for chemical analysis such as identification and composition of the elements in desirable region on a submicrometer scale. Especially, the field emission (FE) type electron source in the electron gun of TEM has been developed recently, and it has been enabled to analyze the chemical composition on a nanoscale, since the electron probe size with the FE type electron gun can be easily converged to less than 1nm compared with conventional thermal filament type electron gun such as tungsten (W) and lanthanum hexaboride (LaB_6). So far, we had investigated the chemical analysis around the interface

and surface in some materials and composite by using TEM with FE type gun. In this chapter, principles of EDS will be overviewed briefly and the validity of the analytical technique with the results for metal/ceramic clad materials and zirconia ceramics focused on their interfaces such as bonding interface, surface of the particles and interphase boundary are shown.
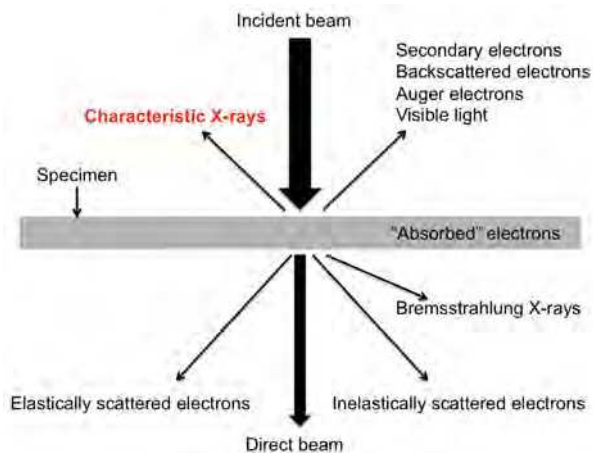

Fig. 1. An interaction of a high voltage electrons and specimen. For a qualitative and quantitative analysis with EDS, characteristic X-rays shown as bold are used.

2. Principles of energy dispersive X-ray spectroscopy

When high voltage electrons traverse a thin foil specimen, one of the primary inelastic interactions is that of inner-shell, ionization as shown in Fig, 2. The ejection of a K-shell electron leaves the atom in an excited state. One of the ways that it can return to ground is by an electron from an outer shell failing to the vacant inner-shell position and at the same time emitting an X-ray of characteristic energy as well as wavelength. This characteristic energy is a function of the difference in electron energy levels of the atom. Thus, it is these X-rays, which we are interested in because they provide direct information about the chemistry of the interaction between the electron and beam. In usual measurement of the EDS, a continuous X-ray is detected as well as characteristic X-rays. The continuous X-ray is emitted with Bremsstrahlung, which is caused by the interaction of the electron beam and a nucleus. In that case, the energy of the incident electrons is changed with the interaction and the extra energy is emitted as a photon. That photon is detected as the continuous X-ray. The continuous X-ray is usually seen as background in the X-ray spectrum. Fig. 3 is the typical EDS profile taken from yttria (Y_2O_3) doped zirconia (ZrO_2), which detail is shown later. Generally, for detection of the characteristic X-ray, silicon-lithium (Si(Li)) semiconductor detectors are used in almost all TEM-EDS as shown in Fig. 4. And they are sealed with different kinds of window consisting of beryllium or an ultrathin polymer to reduce a contamination with hydrocarbons and water vapor from the TEM. And a windowless detector is also used. The ultrathin window and windowless detector can detect the light elements such as B, C, N and O. However, the usual EDS detectors have a disadvantage of relative poor energy resolution, which is approximately 130-140keV in the case of the

conventional Si(Li) type detector. In order to overcome this problem, EDS with a microcalorimeter detector has been developed (Hara et al., 2010), which a superconducting transition-edge-sensor type microcalorimeter is employed as the new detector. This new EDS system will enable to detect with much higher energy resolution of 20eV compared
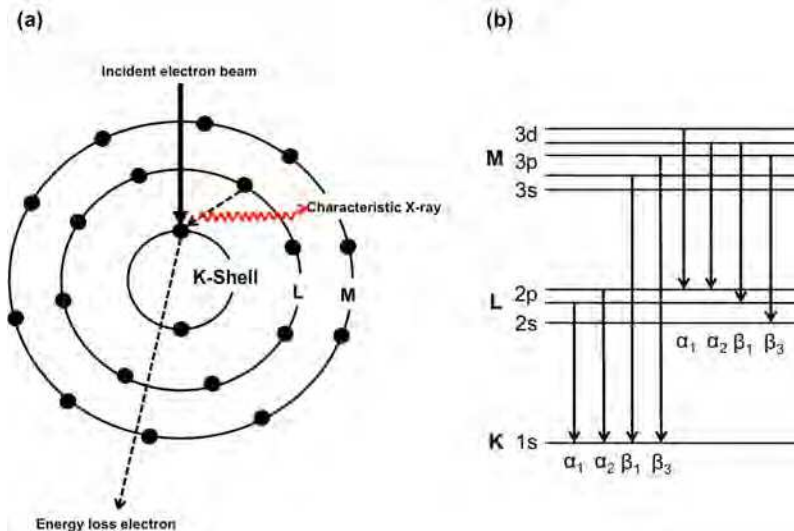

Fig. 2. (a) A schematic illustration of the mechanism of the characteristic X-rays generation. In this illustration, the generated characteristic X-ray corresponds Kα X-ray. (b) A relationship between the kind of characteristic X-ray and energy level of electrons.
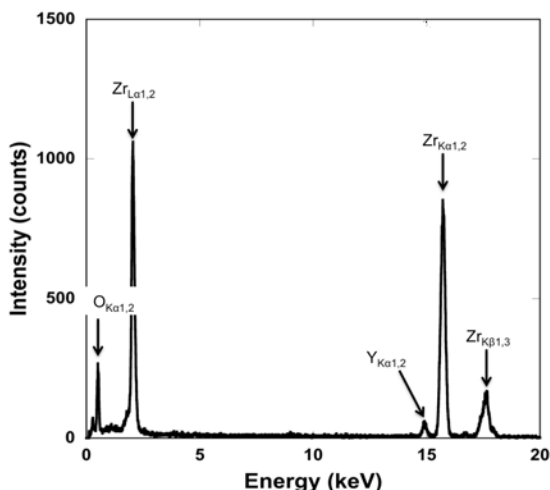

Fig. 3. Typical EDS profile obtained from Y_2O_3 doped ZrO_2.
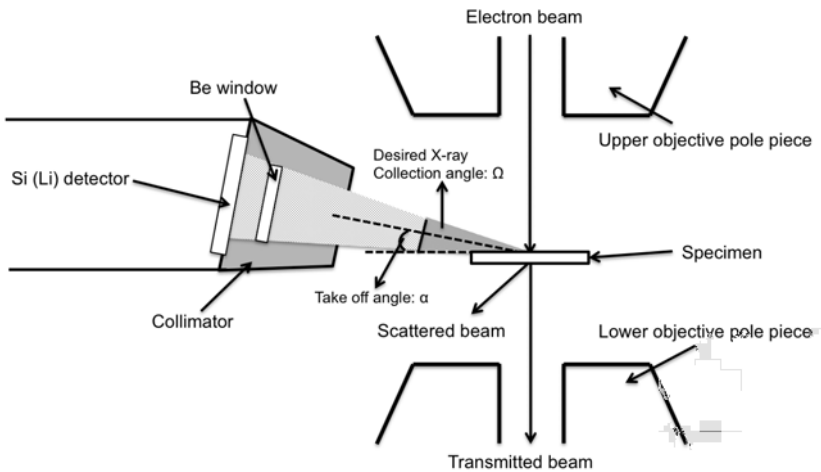
Fig. 4. A schematic drawing of a cross section of EDS detector and objective lens in TEM stage.

with the conventional Si(Li) type detector. Moreover, its detection limit will be improved because of the high sensitivity. As above mentioned, electron beam is interacted with nucleus and electrons of atoms. The behaviors of the interaction in a matter, we can predict with Monte Carlo method. Usually, the extent of the electrons depends of the mass of the matter, i.e., atomic number and is wider with increasing of the atomic number. The extent of the electron is defined as a spatial resolution, which is shown as following equation:

$$b = b_0 + 6.25 \times 10^4 \times \left(\frac{Z}{E_0} \right) \times \left(\frac{\rho}{A} \right)^{1/2} \times t^{3/2} \tag{1}$$

here, b_0 is incident electron probe size, Z is atomic number, E_0 is acceleration voltage, ρ is density of specimen, A is mass number and t is thickness of the specimen, respectively.
By using above equation, spatial resolution of 0.5 to 1 nm can be obtained in TEM with FEG. Most important thing to efficiently detect the X-ray in TEM-EDS is large solid angle Ω shown in Fig. 3, which is schematic illustration of TEM-EDS system and high current density. The solid angle is explained as equation (2),

$$\Omega = \frac{S}{L^2} \tag{2}$$

here, S is cross section of the detector and L is distance between the specimen and the detector, respectively. As shown in eq. (2), the detector should be designed near the

specimen. Recently, the EDS detector in TEM is designed as semi high angle side type. This type detector is well balanced between resolution of image and X-ray detection efficiency. To improve the X-ray detection efficiency, the specimen holder is also devised as well as design of the TEM-EDS instrument.

Quantitative X-ray analysis in the TEM-EDS is one of most straightforward technique. Usual quantitative analysis is used standard sample, which its composition has been already known. And both X-ray intensities in spectra obtained from standard and unknown specimen are compared to each other and quantitative values are estimated. However, since the absorption and fluorescence effect in thin film specimen is less than that in bulk specimen, most of the quantitative analyses in TEM are performed without the measurement of the standard sample and calculated from relative intensity of experimentally obtained each peaks corrected atomic number (Z), absorption (A) and fluorescence (F). Therefore, its analytical method is referred as ZAF (or standardless) method. That is, even if the X-ray correction is simplified, quantitative analysis has been done with high accuracy. In the case of thin film, which thickness is less than several 10 nm, the intensity I_A of characteristic X-ray emitted from specimen A is described as,

$$I_A = \left(I\sigma_A \omega_A a_A N_0 \rho_A C_A \Omega \varepsilon t \right) / M_A \tag{3}$$

here, I is the intensity of the incident beam, σ is ionized cross section of K (or L, M)-shell, ω is fluorescence efficiency, a is intensity ratio of K (or L, M) peak for all K (or M. L) shell, N_0 is Avogadro number, ρ is density, C is atomic composition, Ω is solid angle, ε is detection efficiency, t is thick ness of the specimen and M is atomic weight, respectively. σ_a of K-shell is known as follows:

$$\sigma_A = 4\pi a_0 N_k b_k (R / E_0)(R / E_k)\ln(c_k E_0 / E_k) \tag{4}$$

, which a_0 is Bohr radius, N_k is the number of electrons in K-shell, E_0 is the energy of electrons, E_k is the ionization energy of K-shell, b_k and c_k are constant and R is Rydberg constant, respectively.

Additionally, the fluorescence efficiency ω is also expressed as

$$\omega = Z^4 / (b_k + Z^4) \tag{5}$$

in which, Z is the atomic number. By using above equations (3) to (5), the characteristic X-ray ratio from element A and B is represented as:

$$\frac{I_A}{I_B} = \frac{(\sigma_A \omega_A a_A \rho_A C_A) \cdot M_B}{(\sigma_B \omega_B a_B \rho_B C_B) \cdot M_A} \tag{6}$$

Therefore, between composition and intensity of the X-ray in element A and B is related as follows:

$$\frac{C_A}{C_B} = \frac{(\sigma_B \omega_B a_B \rho_B) \cdot M_A \cdot I_A}{(\sigma_A \omega_A a_A \rho_A) \cdot M_B \cdot I_B} = k_{A,B}\left(\frac{I_A}{I_B}\right) \tag{7}$$

In this equation, $k_{A,B}$ is known as k factor or Cliff-Lorimer factor and composition ratio strongly depends on the k-factor in the experimental EDS measurement. Since the k-factor is

also closely related to the specimen and EDS apparatus, therefore it is quite important to clarify the k-factor with high accuracy in the quantitative EDS analysis. This k-factor is changed daily in actual EDS measurement, because of the different acquirement condition, so that it should be measured for accurate measurement. And in the case of relative thick specimen, absorption correction should be considered. Horita et al., have been proposed k-factor with considering of absorption correction, and they have shown its effectivity (Horita et al., 1998).

3. Experimental chemical analysis with TEM-EDS for elemental distribution

3.1 Chemical analysis in bonding interface of explosively welded metal/ceramic clad materials

Explosive welding technique is one of solid-state welding and clad materials fabricated by this technique have high reliability of the bonding strength (Crossland, 1982). This technique was developed in the 1950s for joining metallic plates. It has been widely used for industry due to its advantage of direct bonding without bonding medium such as braze so far. Nowadays, an application of the explosive welding technique is extended to the field of composite which ductile metals are joined onto brittle materials such as ceramics and metallic glasses as well as metal/metal clad. However, during explosive welding with high-speed deformation, many cracks are introduced and propagated into the brittle   materials and it is serious problem. To overcome that problem, Hokamoto et al. have attempted the metal/brittle materials such as ceramic and metallic glass clad consisted of a metallic foil onto brittle material plate by explosive welding (Hokamoto et al., 1998, 1999, 2010). Especially, they have succeeded the fabrication of metal/ceramics clad materials of several 10 mm without cracks by regulated underwater shockwave (Hokamoto et al., 1998, 1999). In order to understand the bonding mechanism and welding process, it is a key to clarify the bonding interface in the clad. In this chapter, the observation result of the bonding interface between aluminum (Al) and silicon nitride (Si_3N_4) clad material with explosive welding by TEM. And based on the chemical analysis in bonding interface measured by EDS with TEM, the bonding mechanism is also discussed (Ii et al., 2010). Fig. 5 is an external view of explosively welded Al/Si_3N_4 clad. In this experiment, Al of a flyer plate is welded onto Si_3N_4 as a base material. Al is locally deformed, but Al and Si_3N_4 are macroscopically well bonded without macroscopic cracks in both materials. The bright field image around the bonding interface of the clad material is shown in fig. 6. There are also no microscopic cracks around the interface and fine grained layer between Al and Si_3N_4 indicated as intermediate layer in the center of fig. 6. The width of the intermediate layer is approximately 2.5μm. The selected area electron diffraction pattern taken from the region included this intermediate layer is mainly consisted of Debye-Scherrer ring pattern, which is often seen in fine grained polycrystalline. This pattern is also explained without inconsistency, by using the lattice parameter of Al. Therefore, it can be expected that the intermediate layer consist of nanocrystalline Al. In order to clarify the components of the intermediate layer from the chemical viewpoint, EDS measurement and qualification analysis around the interface are performed with scanning TEM (STEM). Although STEM is a type of the TEM, the electron beam of TEM in most of the observations is usually parallel without any convergence. On the other hand, that of the STEM is.
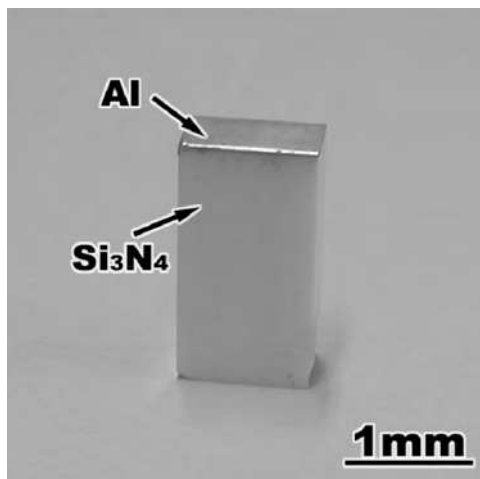
Fig. 5. An outer view of the explosively welded Al/Si_3N_4 clad. In this figure, upper Al as flyer plate is bonded onto Si_3N_4 base material during explosive welding. And no macroscopic cracks are observed.
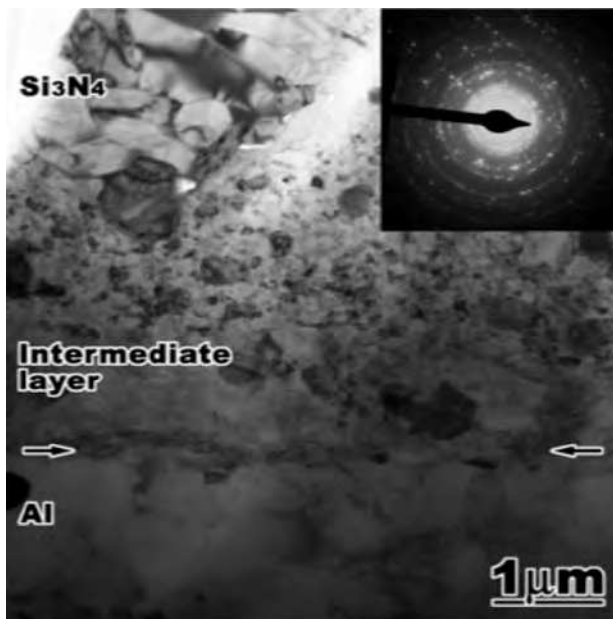

Fig. 6. A Bright field image of the interface of Al/Si_3N_4 clad. A selected area electron diffraction pattern is inserted on the top-right of the image. At the center in this figure, the intermediate layer consisting of a nanocrystalline grain is clearly seen.

illuminated to the specimen with large convergence angle the specimen and scanned in a desirable raster. And the STEM is imaged by the detection of the scattered electron. The detectors in STEM are set to detect the specific scattered electron. Details of STEM are described in elsewhere (Pennycook & Nellist, 2011). Fig. 7 shows the STEM bright field image and the intermediate layer was also clearly observed in fig. 7. Fig. 8 shows X-ray intensity profile across the interface in the Al/Si$_3$N$_4$ clad material obtained by EDS line analysis along the line shown in Fig. 7. Black and red lines correspond to the X-ray intensity of Al-Kα and Si-Kα, respectively. In this figure, the X-ray intensity of the Al-Kα peak is increasing with increase of the distance in fig. 8. Both X-ray intensities of each element are drastically changed at the 0.8μm in this figure, where approximately corresponds to the interface between Si$_3$N$_4$ and nanocrystalline region in the fig.6 and 7. The EDS line profile show that the nanocrystalline region consist of only Al. Many researchers have been reported microstructure around the interface the explosively welded clad materials (Dor-Ram et al., 1979; Kreye et al., 1976; Murdie & Blankenburgs, 1966; Nishida et al., 1993, 1995), so far. Among them, Nishida et al. have precisely investigated the interface of an explosively welded Ti/Ti clad by TEM and found the almost same structure consisting of fine grains. They concluded that the nanocrystallization is caused by the rapid solidification of a thin molten layer formed during the welding (Nishida et al., 1993). In this observation, nanocrystalline region consisting of only Al are also observed. Additionally, melting point of Al is much lower than that of Si$_3$N$_4$, and Al and Si are not solute to each other judging from Al-Si binary equilibrium phase diagram (Murray & McAlister, 1990). Therefore, it can be concluded that nanocrystalline layer is formed with rapid solidification of Al during the explosive welding.
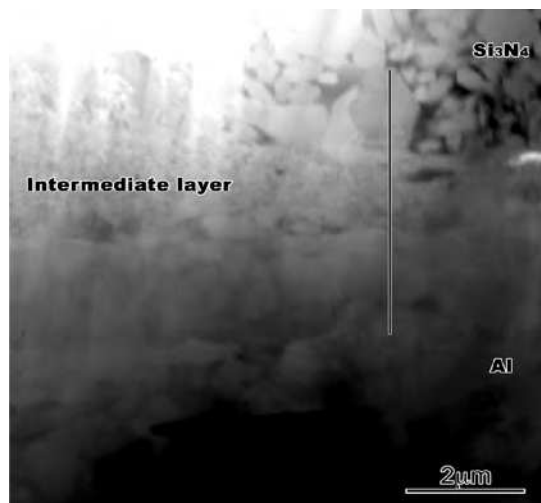

Fig. 7. A STEM image of the interface of Al/Si$_3$N$_4$ clad. EDS line profile shown in Figure 8 was measured along the black line in this figure.
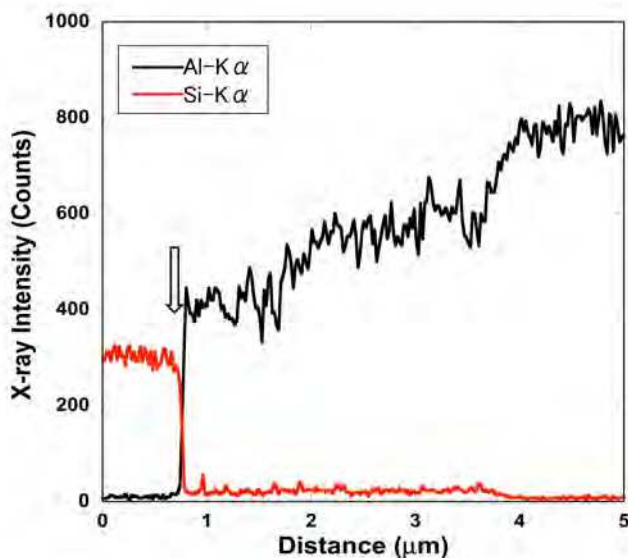
Fig. 8. X-ray intensity profiles of Al-Kα (Black line) and Si-Kα (Red line). Each X-ray intensities are drastically changed at the point shown as arrow. From our systematic analysis, the interface in this clad corresponds to the position where the X-ray intensities are steeply changed.

3.2 Quantitative analysis of surface segregation in Y_2O_3 doped ZrO_2 nano particles

Yttria-stabilized tetragonal zirconia polycrystal (Y-TZP) has proved to be one of important structural ceramic with excellent mechanical properties such as high fracture toughness, strength, and hardness (Gravie et al., 1975; Green et al., 1989). The microstructure and grain growth behavior in sintered bulk Y-TZP have been extensively investigated so far (Ikuhara et al., 1997; Lange, 1988; Lee & Chen, 1988; Sakuma & Yoshizawa, 1992; Yoshizawa & Sakuma, 1989) It has been known that fine grained Y-TZP with the grain size of submicrometer can be obtained because of the formation of cubic and tetragonal two-phase composites. In this case, the tetragonal–cubic phase separation is considered to take place during sintering, and therefore fine grained structure results in stable Y-TZP. In addition, raw ZrO_2 powders with nano-order grain size and good sinterability are commercially available. High-quality Y-TZP powders with narrow particle size distribution can be obtained by the hydrolysis process (Matsui et al., 2002). In previous paper, the microstructural development of the Y-TZP during sintering was investigated by transmission electron microscopy (TEM) observations and energy-dispersive X-ray spectroscopy (EDS) analyses (Matsui et al., 2003), and it was revealed that the yttrium cations tend to segregate in the vicinity of grain boundaries. The relationship between the microstructure of sintered body and the properties of the raw powders have been examined, and it has been pointed out that the microstructure and physical properties of the sintered body strongly depend on the properties of raw powders (Hishinuma et al., 1988). It is therefore crucial to clarify the microstructure and local composition of the

starting powders. In order to clarify whole of the particles on a nano scale, the specimen preparation technique for the high resolution electron microscopy observation has been developed (Ii et al., 2006). In this section, the results of the microstructure and Y^{3+} cation distribution of the Y_2O_3 doped ZrO_2 particles by high-resolution TEM (HRTEM) observations and EDS measurements are shown. Figure 9 (a) shows a typical high-resolution electron micrograph of the yttria-doped zirconia particle. First Fourier Transformed (FFT) pattern of the powder is shown as an inset at the lower-left side in the micrograph. The FFT pattern corresponds to the electron diffraction pattern taken from $[01\bar{1}]$ of the tetragonal phase and it indicates that the particle is tetragonal single phase. Fig. 9 (b) and (c) show an enlarged lattice image of the surface and internal region as indicated by B and C in (a), respectively. As shown in Figs. 9 (b) and (c), the two-dimensional lattice fringe is clearly observed inside the particle. Figure 10 shows the composition of Y_2O_3 analyzed from EDS spectra as a function of distance from the surface of the particle. The error bars to each measuring point are also shown. In this EDS measurements, the spectra obtained from this particle and the quantitative analysis have high reliability, because the thickness of the specimen is thin enough to obtain the lattice image into the internal region and uniform. In Fig. 10, the error is within 0.3% of each estimated value, and it is relatively small compared with the estimated Y_2O_3 composition. Both the Y_2O_3 compositions take on the maximum value at the surface of the particle, but suddenly reduce at a distance of 1 nm off from the surface. The Y_2O_3 composition increases again with increasing distance from the surface, but takes on a constant value over the distance of 5 nm. This fact suggests that Y^{3+} cations migrate from 1 nm inside to the surface of the particle and segregate at the surface.
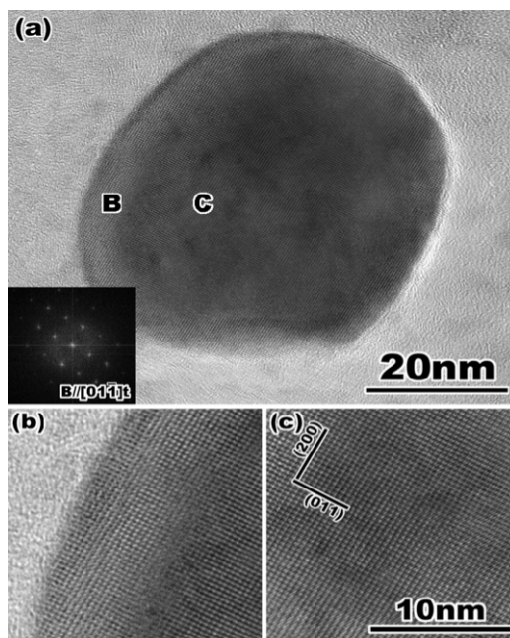

Fig. 9. (a) A high resolution TEM image of Y_2O_3 doped ZrO_2 particle. The FFT pattern in (a) indicates that the particle is tetragonal single phase. (b) and (c) Enlarged lattice image of the surface and the internal region of the particle indicated by B and C in (a), respectively.

In the case of grain boundary in polycrystalline Y_2O_3 doped ZrO_2, dopant cations have been reported to segregate at the vicinity of the grain boundary over the width of several nm to reduce excess grain boundary energy (Ikuhara et al., 1997; Shibata et al., 2004). The present results are obtained in a situation such that the surface excess energy is reduced by surface segregation of the Y^{3+} cations. The observation of the other particles also showed almost same tendency. On the other hand, some of the particles, which the tetragonal phase transforms to the monoclinic phase, have a uniform distribution of Y_2O_3 contents, and that the formation of monoclinic phase is not attributed to Y_2O_3 inhomogeneous distribution. The stability of the monoclinic phase of ZrO_2 has been reported to depend on the grain size; the tetragonal phase of ZrO_2 with the grain size of less than 500 nm cannot be thermally transformed to monoclinic phase (Gupta et al., 1978; Sakamoto, 1990). Since the average size of the present zirconia particle is approximately 50 nm, the formation of monoclinic zirconia cannot be explained from a thermomechanical point of view. Moreover, the monoclinic phase was observed in the vicinity of the surface. Therefore, the monoclinic phase is probably formed by stress-induced transformation during the milling process, which was performed in the final stage of the powder fabrication.
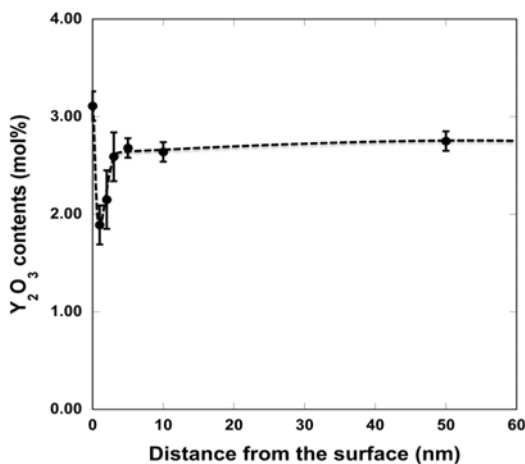

Fig. 10. A composition of Y_2O_3 estimated by quantitative analysis of EDS spectra in Y_2O_3 doped ZrO_2 particle as a function of the distance from the surface.

3.3 Yttrium cation distribution at cubic and tetragonal interphase boundary in Y-TZP

As abovementioned, Y_2O_3 stabilized tetragonal ZrO_2 polycrystal (Y-TZP) is one of the technologically important structural ceramics. For the development of the Y-TZP bulk materials, the microstructural development including phase transformation and grain growth in Y-TZP has been widely investigated by many researchers so far (Gravie et al., 1975; Lange, 1988; Lee & Chen, 1988; Yoshizawa & Sakuma, 1989). Their most important aspects of the relationship between the phase transformation and grain growth were that grain growth in the tetragonal (t) and cubic (c) dual-phase region is slower than t or c single phase region. For instance, the grain growth behavior in 4mol% Y_2O_3-stabilized ZrO_2 was explained in terms of the pinning-effect of cubic phase grains dispersed in TZP (Yoshizawa & Sakuma, 1989). However, it should be noted that their phenomenological analysis was

based on the assumption that the ZrO_2-Y_2O_3 in t and c two-phase region was dual-phase composite consisting of t- and c-grains. On the other hand, Ikuhara *et al.* (1997) investigated the microstructure in TZP by high resolution transmission electron microscopy (HRTEM) and energy dispersed x-ray spectroscopy (EDS), and found that Y^{3+} cations are segregated over a width of 4-6 nm across the boundaries in TZP. More recently, the detailed microstructural change during sintering process in TZP has been investigated and a formation of the cubic phase from grain boundary due to the Y^{3+} cation's segregation and its growing to the grain interior are found (Matsui et al., 2003, 2006). Thus, this tetragonal to cubic phase transformation is termed as grain boundary segregation induced phase transformation (GBSIPT). Through the GBSIPT, the interphase boundary between the front of the cubic phase and the tetragonal matrix, i.e. c/t interphase boundary is likely to form inside grains. The lattice parameter ratio is slightly different between tetragonal and cubic phases, whose lattice mismatch of two phases is less than 1%. Therefore, it can be expected that the interphase boundary is coherent or semi-coherent boundary. In the case of the semi-coherent boundary, the excess strain interface energy is released by introducing misfit dislocation. In this section, the relationship between the interphase boundary structure and yttrium cation distribution in Y-TZP is focused. Fig. 11 (a) shows a typical microstructure observed in the Y-TZP specimen sintered at 1650°C. As shown in Fig. 11 (a), the dot-like contrasts between two arrows are periodically observed inside the grain.
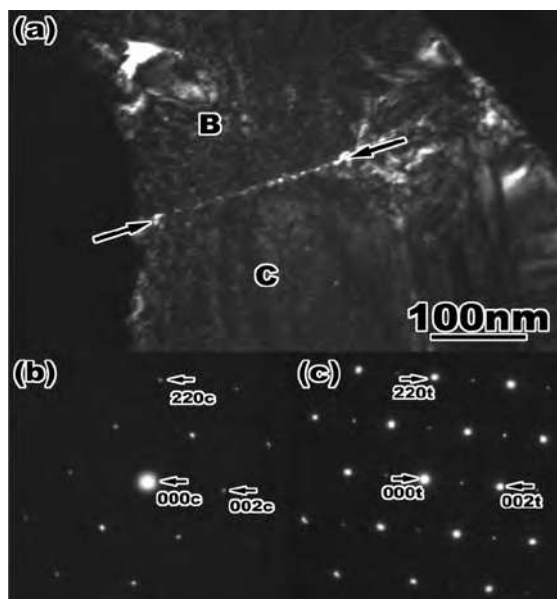

Fig. 11. (a) A Dark field image of typical microstructure of sintered Y_2O_3 stabilized ZrO_2 tetragonal zirconia polycrystal. This image were slightly tilted to keep the two beam excitation condition with g = (110)$_{c,t}$ and see misfit dislocations clearly. (b) and (c) Selected area electron diffraction patterns taken from B and C indicated in (a). The incident electron beam direction is parallel to [1 $\bar{1}$ 0]$_{c,t}$. And these diffraction patterns show cubic in (b) and tetragonal (c) single phase, respectively.

Fig. 11 (b) and (c) show selected electron diffraction patterns taken from the region marked by B and C in Fig. 11 (a), which indicates the interface is formed between cubic (Fig. 11 (b)) and tetragonal (Fig. 11 (c)) phase, respectively. Therefore, we considered that their dot-like contrasts are on the interface. The average interval of these contrasts is estimated to be approximately 10 nm. An arrangement of the periodic contrast was confirmed to be close to near <111> direction from the result of the trace analysis in the obtained TEM micrograph and electron diffraction patterns. In addition, it was also confirmed that the plane normal of this interface, which is the periodic contrast along near <111> direction, is close to the <22$\bar{1}$>t and c, respectively. Consequently, it is predicted that the interphase boundary observed in this specimen is near {22$\bar{1}$}t and {22$\bar{1}$}c, respectively. In order to investigate the detailed interphase boundary structure, especially misfit dislocation structure on an atomic level, HRTEM observations for the c/t interphase boundary have been done and revealed that the misfit dislocations at the c/t interphase boundary are clearly observed (Ii et al., 2008). Fig. 12 shows the profile of the Y_2O_3 contents from EDS spectra as a function of distance from the c/t interphase boundary in Y-TZP. The Y_2O_3 contents take the uniform value both in the cubic and tetragonal regions, but steeply changes across the c/t interphase boundary. The steeply sloped change in the Y_2O_3 contents is in good agreement with the fact that the misfit dislocations are introduced by the difference in the lattice parameter between c and t phases with different Y^{3+} compositions. It should be noted that the yttrium distribution is almost uniform inside the grain in the bulk Y-TZP sintered at 1300°C. The present results indicate that Y^{3+} cation redistribution takes place in association with tetragonal-cubic phase transformation in Y-TZP.
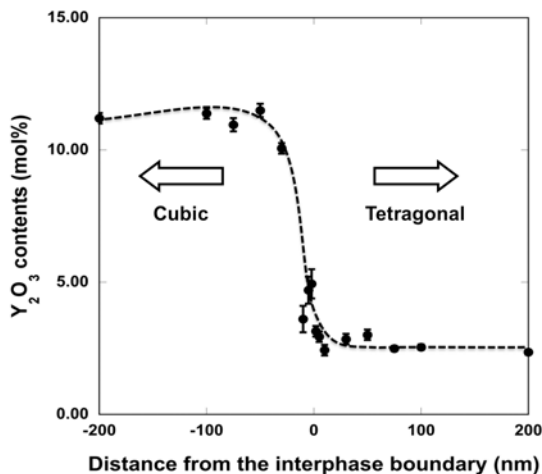

Fig. 12. A Y_2O_3 contents profile obtained by EDS spectra across the c/t interphase boundary as a function of the distance from the boundary.

4. Conclusion

In this chapter, the principles of EDS are briefly described and some results of the nanoscale chemical analysis at many interfaces measured by EDS installed to TEM with field emission

type electron gun, whose probe size is less than less than 1nm. In the bonding interface in the explosively welded Al/Si$_3$N$_4$ clad materials, element distribution around the interface was measured by TEM and STEM-EDS as well as microscopic characterization. For this purpose, TEM and STEM observation revealed that the intermediate layer with approximately 2.5 μm between the Al and Si$_3$N$_4$ exists and this layer consists of fine grains whose average diameter of 100nm. And the intermediate layer consists of only Al from selected area electron diffraction pattern and EDS measurement across the interface. Consequently, we clarified that the fine grained Al is formed by rapid solidification after melting during the cladding and it plays as an important role to the welding of Al and Si$_3$N$_4$. On the other hand, the microstructures of Y$_2$O$_3$ doped ZrO$_2$ nano particles were also observed by HRTEM and the distribution of Y$_2$O$_3$ inside particle was measured by EDS. The experimental technique for the observation of whole particle with the size of several 100 nm was developed and the surface segregation of Y$_2$O$_3$ was detected within a few nm from the surface for the relaxation of the excess surface energy. The interphase boundary between the front of grown cubic and tetragonal matrix in sintered Y-TZP was investigated by CTEM and HRTEM with EDS measurement. Y^{3+} cation concentration is drastically changed at the c/t interphase boundary. Since the periodic misfit dislocations are also observed at the c/t interphase boundary, therefore, the steep change in Y^{3+} cation composition must cause the misfit strain at the interphase boundary, and consequently leads to introduce misfit dislocations. These results will provide the effectivity of the EDS measurement combined with TEM for the chemical analysis of advanced materials on the nano scale and the guidelines for understanding the correlation between the microstructure observation and the nano scale analysis.

5. Acknowledgment

6. References

Brydson, R. (2001). *Electron Energy Loss Spectroscopy*, Tayler & Francis, ISBN 1-85996-134-7, New York

Crossland, B. (1982). *Explosive Welding of Metels and its application* (Clarendon press, London 1982) ISBN 0-19-859-119-5..

Dor-Ram, B.; Weiss, Z. & Komen, Y. (1979). Explosive cladding of Cu/Cu systems: An electron microscopy study and a thermomechanical model, *Acta Metall.*, Vol. 27 Iss.9, pp. 1417-1429

Edington, J.W. (1974). *Practical Electron Microscopy in Materials Science*, MacMillan, Philips Technical Library, Eindhoven. Reprinted by Ceramic Book and Literature Service, ISBN 978-1878907356, Marietta, Ohio

Egerton, R. F. (1996). *Electron Energy-Loss Spectroscopy in the Electron Microscope*, 2nd edition, Plenum Press, ISBN 0-306-45223-5, New York

Fultz, B & Howe, J.M. (2002). *Transmission Electron Microscopy and Diffractometry of Materials*, 2nd ed., Spinger-Verlag, ISBN 978-3-540-73885-5, Berlin

Garvie, R. C.; Hannink, R. H. J. & Pascoe, R.T. (1975). CERAMIC STEEL, *Nature*, Vol.258, pp.703-704.

Green, D. G.; Hannink, R. H. J. and Swain, M. V. (1989). *Transformation Toughening of Ceramics*. CRC Press, Boca Raton, ISBN 978-0849365942, FL, 1989.

Gupta, T. K.; Bechtold, J. H.; Kuznicki, R. C.; Cadoff, L. H. & Rossing, B. R. (1977). Stabilization of Tetragonal Phase in Polycrystalline Zirconia, *J. Mater. Sci.*, Vol.12, pp.2421–2426.

Gupta, T. K.; Lange, F. F. & Bechtold, J. H. (1978). Effect of Stress-Induced Phase Transformation on the Properties of Polycrystalline Zirconia Containing Metastable Tetragonal Phase, *J. Mater. Sci.*, Vol.13, pp.1464–1470

Hammeeschmidt, M & Kreye, H. in: *Shock Waves and High-Strain-Rate Phenomena in Metals (Concepts and Applications)*, edited by M. A. Meyers and L. E. Murr, Plenum Pless, New York (1981), 961. 978-0306406331

Hara, T.; Tanaka, K.; Maehata, K.; Mitsuda, K.; Yamasaki, N. Y.; Ohsaki, M.; Watanabe, K,; Yu, X,; Ito, T, & Yamanaka, Y. (2010) Microcalorimeter-type energy dispersive X-ray spectrometer for a transmission electron microscope. *Journal of Electron Microscopy*, Vol.59, No.1, pp.17–26

Hishinuma, K.; Kumai, T.; Nakai, Z.; Yoshimura, M. & Somiya, S. Characterization of Y_2O_3–ZrO_2 Powders Synthesized Under Hydrothermal Conditions, *Adv. Ceram.*, Vol.24, pp.201–209.

Hokamoto, K.; Fujita, M. & Shimokawa, H. (1998). Explosive Welding of a Thin Metallic Plate onto a Ceramic Plate Using Underwater Shock Wave, *Rev. High Pressure Sci. Technol.* Vol. 7 (1998), pp.921-923.

Hokamoto, K.; Fujita, M.; Shimokawa, H. & Okugawa, H. (1999). A new method for explosive welding of Al/ZrO_2 joint using regulated underwater shock wave, *J. Mater. Proc. Tech.* Vol.85, No.1-3, pp.175-179.

Hokamoto, K.; Nakata, K.; Mori, A.; Ii, S.; Tomoshige, R.; Tsuda, S.; Tsumura, T.; Inoue, A. (2009). Microstructural characterization of explosively welded rapidly solidified foil and stainless steel plate through the acceleration employing underwater shock wave, *Journal of Alloys and Compounds*. Vol.485, pp.817–821

Horita, Z. (1998). Quantitative X-ray Microanalysis in Analytical Enectron Microscopy, *Mater. Trans. JIM*, Vol.39, No.9, pp.947-958.

Ii, S.; Yoshida, H.; Matsui, K.; Ohmichi, M. & Ikuhara, Y. (2006) Microstructure and Surface Segregation of 3mol% Y_2O_3 doped ZrO_2 particle, *J. Am. Ceram. Soc.*, Vol.89, No.7, pp.2952-2955.

Ii, S.; Yoshida, H.; Matsui, K. & Ikuhara, Y. (2008). Misfit Dislocation Formation at the c/t Interphase Boundary in Y-TZP, *J. Am. Ceram. Soc.*, Vol.91 No.11, pp.3810–3812

Ii, S.; Iwamoto, C.; Satonaka, S.; Hokamoto, K. & Fujita, M. (2010). Microstructure of Bonding Interface in Explosively Welded Metal/Ceramic Clad, Mater. Sci. Forum., Vols.638-642, pp.3775-3780.

Ikuhara, Y.; Thavorniti, P. & Sakuma, T. (1997). Solute Segregation at Grain Boundaries in Superplastic SiO2-Doped TZP, *Acta Mater.*, Vol.45, pp.5275–5284.

Kreye, H.; Wittkamp, I. & Richter, U. (1976). Electron Microscope Investigation of the Bonding Mechanism in Explosive Bonding. *Zeitschrift fuer Metallkunde*, Vol.67, Iss.3, pp. 141-147. ISSN: 00443093,

Lange, F. F. (1988). Controlling Microstructures Through Phase Partitioning from Metastable Precursors The ZrO_2–Y_2O_3 System, pp. 519–532 in Ultrastructure Processing of Advanced Ceramics, Edited by J. D. Mackenzie and D. R. Ulrich. Wiley, New York, 1988.

Lee, I. G. & Chen, I. -W. (1988). Sintering and Grain Growth in Tetragonal and Cubic Zirconia, *Sintering '87.* pp. 340–345 in, Edited by S. Somiya, M. Shimada, M. Yoshimura, and R. Watanabe. Elsevier Applied Science, ISBN 978151662906, London, 1988.

Matsui, K. & Ohgai, M. (2002). Formation Mechanism of Hydrous Zirconia Par- ticles Produced by Hydrolysis of ZrOCl2 Solutions: IV, Effects of $ZrOCl_2$ Concentration and Reaction Temperature, *J. Am. Ceram. Soc.*, Vol.85, pp.545–553.

Matsui, K.; Horikoshi, H.; Ohmichi, N.; Ohgai, M.; Yoshida, H. & Ikuhara, Y. (2003). Cubic-Formation and Grain-Growth Mechanisms in Tetragonal Zirconia Poly- crystal, *J. Am. Ceram. Soc.*, Vol.86, pp.1401–1408.

Matsui, K.; Ohmichi, N.; Ohgai, M.; Yoshida, H.; & Ikuhara, Y. (2006). Effect of alumina-doping on grain boundary segregation-induced phase transformation in yttria-stabilized tetragonal zirconia polycrystal, *J. Mater. Res.,* Vol.21, pp.2278-2289

Murray, J. L. & McAlister, M. J. in: *Binary Alloy Phase Diagrams*, II Ed., edited by T.B. Massalski, Vol. 1 (1990), p 211-213

Murdie, D.C. & Blankenburgs, G. (1966). Examination of Two Explosively Welded Interfaces, *J. Inst. Met.*, Vol.94 (1966), 119-120.

Nishida, M.; Chiba, A.; Imamura, K.; Minato, H. & Shudo, J. (1993). Microstructural modifications in an explosively welded Ti/Ti clad material: I. Bonding interface, *Metall. Trans. A*, Vol. 24A, No.3, pp.735-742

Nishida, M.; Chiba, A.; Honda, Y.; Hirazumi, J. & Horikiri, K. (1995). Electron microscopy studies of bonding interface in explosively welded Ti/steel clads, *ISIJ Int.*, Vol.35, Iss.2, pp.217-219

Pennycook, S. J. & Nellist, P. D. (2011). Scanning Transmission Electron Microscopy, Springer-Verlag, ISBN 978-1441971999, New York.

Sakamoto, M. (1990). Raw Powder of ZrO_2 System, pp. 265–273 in Technical Hand- book of Super Fine Ceramic, Edited by S. Shirasaki and A. Makishima. Science Forum, Tokyo, 1990 (in Japanese).

Sakuma, T. & Yoshizawa, Y. (1992). The Grain Growth of Zirconia During Annealing in the Cubic/Tetragonal Two-Phase Region, *Mater. Sci. Forum.*, Vol.94–96, pp.865–870 (1992).

Shibata, N.; Oba, F.; Yamamoto, T. & Ikuhara, Y. (2004). Structure, Energy and Solute Segregation Behavior of [110] Symmetric Tilt Grain Boundaries in Yttria- Stabilized Cubic Zirconia, *Philos. Mag.*, Vol.84, pp.2381–2415.

Wiliams, D.B. & Carter, C. B. (1996). *TRANSMISSION ELECTRON MICROSCOPY: a textbook for materials science*, Plenum Press, ISBN 0-306-45247-2, New York

Yoshizawa, Y. & Sakuma, T. (1989). Evolution of Microstructure and Grain Growth in ZrO_2–Y_2O_3 Systems, *ISIJ Int.*, Vol.29, pp.746–752.
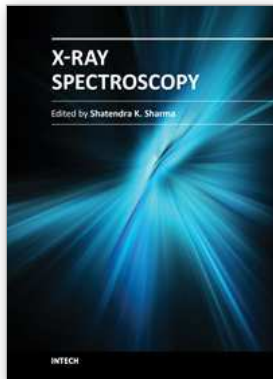
X-Ray Spectroscopy

Edited by Dr. Shatendra K Sharma

The x-ray is the only invention that became a regular diagnostic tool in hospitals within a week of its first observation by Roentgen in 1895. Even today, x-rays are a great characterization tool at the hands of scientists working in almost every field, such as medicine, physics, material science, space science, chemistry, archeology, and metallurgy. With vast existing applications of x-rays, it is even more surprising that every day people are finding new applications of x-rays or refining the existing techniques. This book consists of selected chapters on the recent applications of x-ray spectroscopy that are of great interest to the scientists and engineers working in the fields of material science, physics, chemistry, astrophysics, astrochemistry, instrumentation, and techniques of x-ray based characterization. The chapters have been grouped into two major sections based upon the techniques and applications. The book covers some basic principles of satellite x-rays as characterization tools for chemical properties and the physics of detectors and x-ray spectrometer. The techniques like EDXRF, WDXRF, EPMA, satellites, micro-beam analysis, particle induced XRF, and matrix effects are discussed. The characterization of thin films and ceramic materials using x-rays is also covered.

How to reference

In order to correctly reference this scholarly work, feel free to copy and paste the following:

INTECH
open science | open minds